Journal of Materials Chemistry A

Accepted Manuscript

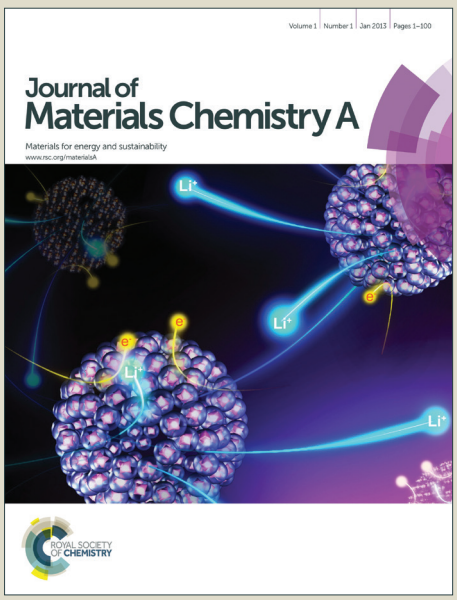

ROYAL SOCIETY OF CHEMISTRY

www.rsc.org/materialsA

Graphical Abstract

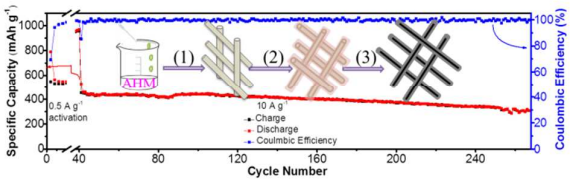

A new approach is used to synthesis MoO_2@C, with excellent capacity, rate capability and cycle stability for LIBs.

Cite this: DOI: 10.1039/c0xx00000x

www.rsc.org/xxxxxx

ARTICLE TYPE

A new approach to synthesize MoO_2@C for high-rate lithium ion batteries

Ying Wang[a,b], Zhenguo Huang[b*], Yijing Wang[a*]

Received (in XXX, XXX) Xth XXXXXXXXX 20XX, Accepted Xth XXXXXXXXX 20XX

DOI: 10.1039/b000000x

MoO_2@C nanocomposite was prepared using oleic acid to reduce the MoO_3 precursor and to simultaneously coat the resultant one-dimensional MoO_2 nanorods with carbon layers. The MoO_2@C composite has a mesoporous structure with a surface area of 45.7 $m^2 \cdot g^{-1}$, and a typical pore size of 3.8 nm. When applied as an anode for lithium ion batteries, the MoO_2@C electrode exhibits not only high reversible capacity, but also remarkable rate capability, and excellent cycling stability. A high capacity of 1034 mAh·g^{-1} was delivered at 0.1 A·g^{-1}. And at a super-high specific current of 22 A·g^{-1}, a capacity of 155 mAh·g^{-1} was still obtained. When cycled at 0.5 and 10 A·g^{-1}, the Li/MoO_2@C half cells retained 861 and 312 mAh·g^{-1} capacity after 140 and 268 cycles, respectively. The mesoporous nature of the MoO_2@C nanocomposite and the thin-layer carbon coating are believed to contribute to the enhanced electrochemical performance, which not only feature the efficient four-electron conversion reaction for Li^+ storage, but also effectively tolerate volume expansion during the cycling.

Introduction

Lithium-ion batteries (LIBs), featuring efficient Li^+ shuttle between the anode and cathode and consequently delivering high energy and power density, have shown huge potential for applications in the fields of grid-level electricity storage and electric vehicles.[1-5] Currently, one of the most crucial challenges for future application of LIBs is how to design and fabricate new anode materials with high capacity, good rate-capability, long-life cycling stability, and low cost.[6, 7] To achieve this goal, a plethora of materials have been studied, including metal oxides,[8, 9] carbon materials,[10, 11] and various alloys.[12, 13] Among all these materials, MoO_2 has recently emerged as a particularly interesting candidate, since it has low electrical resistivity, high electrochemical activity towards lithium, and a relatively low price.[14-18]

Bulk MoO_2 is known to react with Li^+ via insertion/de-insertion process, as shown in Eq. (1), which results in a low theoretical capacity of 209 mAh·g^{-1}.[19] This process is accompanied by severe volume expansion during the cycling, which leads to serious pulverization and consequent rapid capacity fading.[20] In general, there are several ways to improve the electrochemical performance of electrodes. First, nano-sizing can effectively improve surface areas, shorten diffusion distances, and provide more active sites.[3, 9, 21] Mesoporous materials have also drawn great attention, since they provide extra pores to effectively buffer the volume change during cycling and facilitate the contact between the electrolyte and the active materials. Carbon coating is another effective method to accommodate the volume change and also to improve the electron conductivity.[22]

$$MoO_2 + xLi^+ + xe^- \leftrightarrow Li_xMoO_2 (0 < x < 1) \quad \text{Eq. (1)}$$

$$MoO_2 + 4\,Li^+ + 4e^- \leftrightarrow Mo + 2Li_2O \quad \text{Eq. (2)}$$

In the case of MoO_2 electrode, the lithiation/delithiation of nanostructured MoO_2 features a transformation from insertion to conversion type (Eq. (2)).[14, 23] Therefore, the theoretical capacity of nanostructured MoO_2 is 838 mAh·g^{-1}, about four times larger than that of bulk MoO_2. Currently, various types of nano-sized MoO_2 (e.g. particles,[24, 25] tubes,[23] spheres,[26-29] mesoporous rods[30]) have been prepared and showed improved electrochemical performance. To overcome the volume expansion and the resulting performance degradation, MoO_2-carbon composites with different morphologies and architectures, have also been fabricated. For example, Hu *et al.* reported the electrochemical performance of MoO_2/graphene oxide with a capacity of 310 mAh·g^{-1} after 35 cycles at 0.5 A·g^{-1};[16, 17] while the MoO_2/3D-graphene composites, reported by Huang's group, delivered 975.4 and 537.3 mAh·g^{-1} capacities at 0.05 and 1 A·g^{-1} specific currents, respectively.[18] MoO_2@C/graphene reported by Guo et al. showed a high capacity of 500 mAh·g^{-1} after 200 cycles at 5 A·g^{-1}.[15]

The above-mentioned results indicate that it is crucial to develop a controllable and selective method for preparing mesoporous MoO_2/C composite. Herein, we present a new approach to prepare mesoporous MoO_2@C via an oleic acid assisted annealing process. Different from the previous reports, which general involved additional carbon source or templates,[16, 17, 27, 31-33] herein, the mixture of nanorods MoO_3 and oleic acid enables a

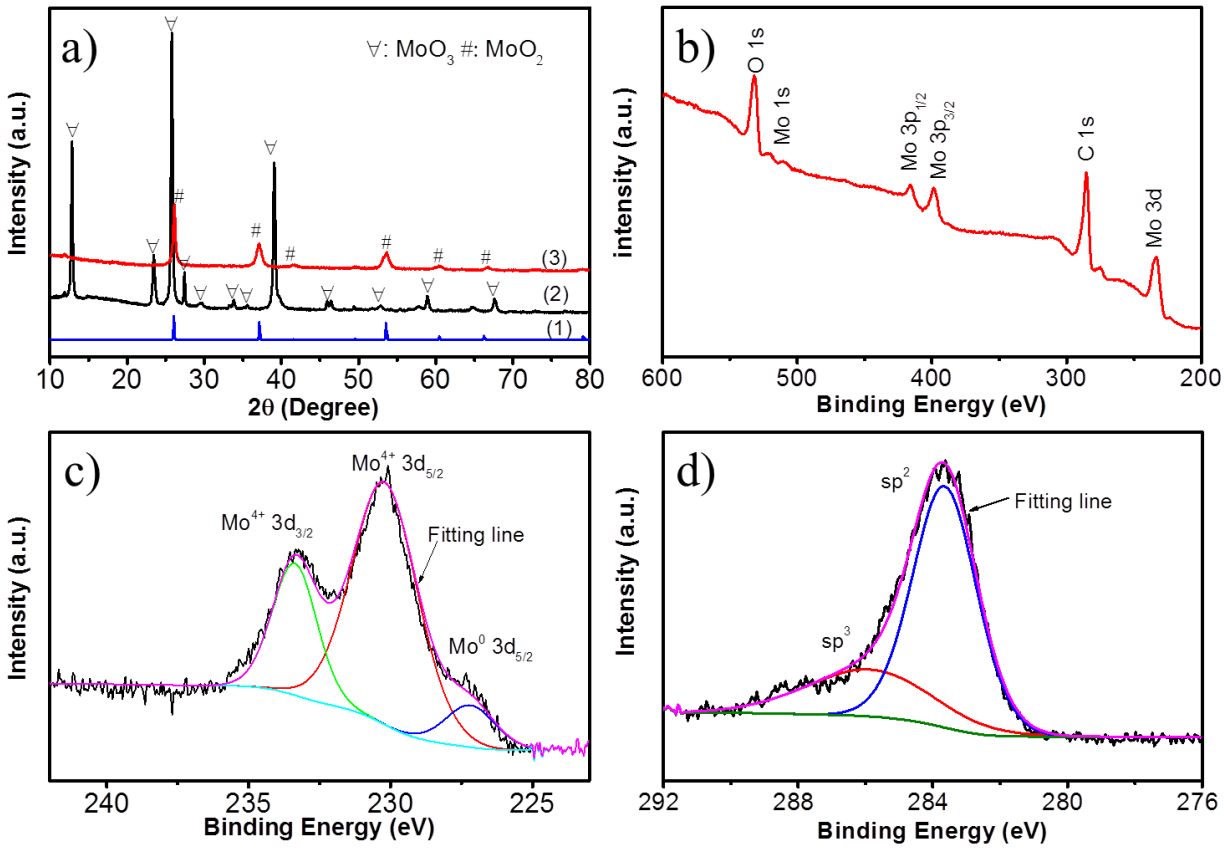

Fig. 1 (a) XRD patterns of (1) standard MoO_2 (JCPDS: 65-5787), (2) MoO_3 precursor, and (3) as-obtained MoO_2@C; (b) XPS survey of the as-obtained MoO_2@C; high resolution XPS spectra of (c) Mo 3d and (d) C 1s

simultaneous reduction and carbon thin film formation under mild conditions. Electrochemical investigations indicate that the as-obtained MoO_2@C exhibits excellent battery performance as LIBs anode, with superior high reversible capacity, long-life cycling stability, and remarkable rate capability

Experimental section

Preparation of MoO_2@C nanocomposite

MoO_3 precursor was synthesized following a previous report with minor modifications.[34] Typically, 5 mL saturated aqueous solution of $(NH_4)_6Mo_7O_{24}$ (denoted as AHM, Sigma Aldrich) was acidified to pH 5 using 2.2 M HNO_3, and then aged for 4 weeks. After adding another 10 mL 2.2 M HNO_3, the AHM solution was transferred into a Teflon-lined autoclave and kept at 200 °C for 9 h in an oven. The precipitation was washed with distilled water and collected by centrifugation, and then vacuum dried at 80 °C overnight. To prepare the MoO_2@C, the MoO_3 precursor was first soaked in oleic acid for more than 24 h. The viscous mixture was then centrifuged to remove extra oleic acid. Finally, the powders were transferred into a tube furnace and calcined at 500 °C for 4 h under flowing Ar. After naturally cooling down to room temperature, the MoO_2@C was obtained. Commercial available MoO_2 (Sigma Aldrich) was used for comparison.

Characterization

X-ray diffraction (XRD, GBC eMMA), X-ray photoelectron spectroscopy (XPS, VG Scientific ESCALAB 2201XL), gas adsorption/desorption isotherm analysis (NOVA 2200e, Quantachrome), thermogravimetric analysis (TGA, Mettler Toledo TGA/DSC1), scanning electron microscopy (SEM, JEOL JSM7500FA), and transmission electron microscopy (TEM), high-resolution TEM (HR-TEM, JEOL JEM-ARM200F) measurements were carried out to determine the structure, composition, and morphology of the as-obtained samples.

Electrochemical measurements

The electrochemical performances were evaluated by using standard 2032 type coin cells. Active materials, carbon black (Cabot Australasia PTY Ltd.), and poly(vinylidene fluoride) (PVDF, Sigma Aldrich) were mixed in a weight ratio of 8:1:1, and dispersed in N-methylpyrrolidone (NMP) solution, and then ball milled for 30 min to form a slurry. The slurry was cast onto copper foil using a doctor blade and vacuum dried at 120 °C overnight. A lithium disc (MTI Corporation) was used as the counter electrode. 1 M $LiPF_6$ (Sigma Aldrich) in ethylene

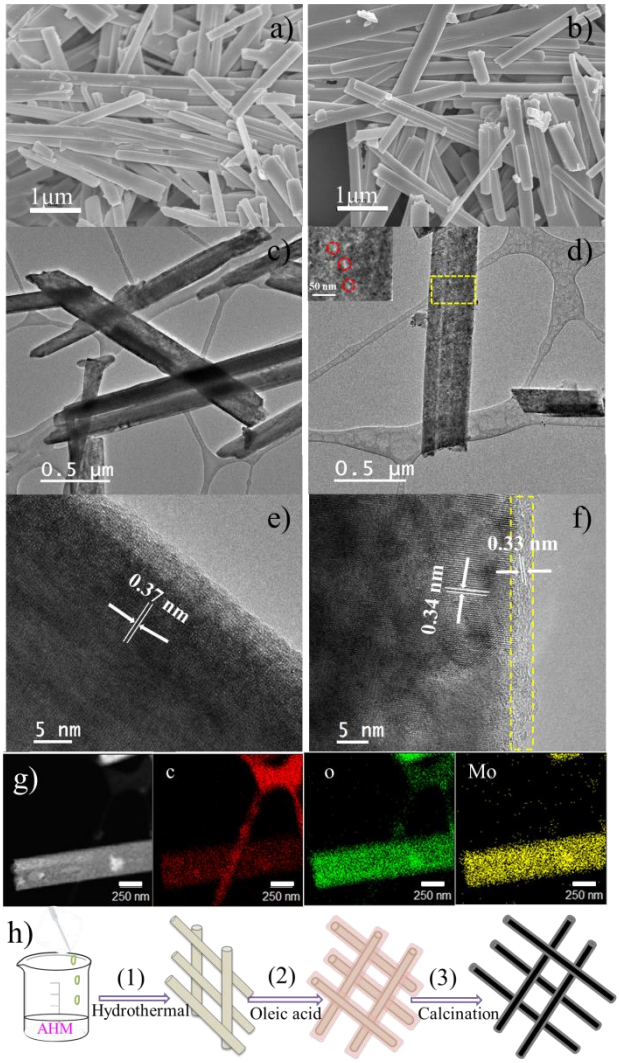

Fig. 2 SEM, TEM and HR-TEM images of (a, c, e) MoO_3 precursor and (b, d, f) the as-obtained MoO_2@C; (g) dark field TEM image of the MoO_2@C and the corresponding elemental mappings for C (red), O (green), and Mo (yellow). (h) Illustration of the synthesis procedure of the MoO_2@C nanorods. Inset d) is an enlarged view of selected area (yellow rectangle), and the red circles highlight some typical pores in the MoO_2@C. The dashed yellow rectangle in f) indicates the carbon layer.

carbonate (EC, Sigma Aldrich), dimethyl carbonate (DMC, Alfa Aesar), and diethyl carbonate (DEC, Alfa Aesar) (3:4:3 by volume), with the addition of 5 % fluorinated ethylene carbonate (FEC, Sigma Aldrich, for capacity retention [35]) was used as the electrolyte. Polypropylene (PP, MTI Cooperation) was used as the separator. The cells were assembled in an argon-filled glove box with the oxygen and water content below 1 ppm. Galvanostatic charge-discharge tests were carried out at room temperature on a battery testing system (Shenzhen NEWARE Battery, China) in the potential range of 0.01-3.00 V (vs. Li^+/Li). Cyclic voltammetry (CV) tests and electrochemical impedance spectroscopy (EIS) measurements were performed on a Biologic VMP-3 electrochemical work station.

Results and Discussion

Structure and morphology characterization

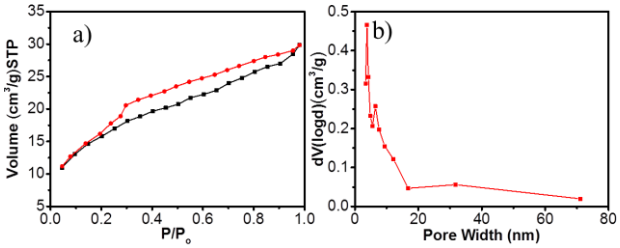

Fig. 3 (a) Typical N_2 adsorption/desorption isotherms, and (b) pore size distribution plot of the MoO_2@C nanorods.

Table 1 BET surface areas and pore diameter distributions.

Sample name	BET surface area ($m^2 \cdot g^{-1}$)	Pore diameter (nm)
MoO_2 (commercial)	1.1	4.2
MoO_3	8.1	5.6
MoO_2@C	45.7	3.8

The crystallinity and purity of the MoO_3 precursor and the as-obtained MoO_2@C were determined by XRD (Fig. 1a). For the MoO_3 precursor, all the reflections match well with standard α-MoO_3.[34] Reflections of the calcined powders can be indexed to monoclinic MoO_2 phase (JCPDS: 65-5787), confirming the formation of high purity MoO_2. The broad reflections in the MoO_2@C indicate a small crystallite size. According to the Scherrer equation, the average crystal size is 13.7 nm (based on the (110) plane), which would be conducive toward Li^+ storage.[24, 31] XPS was used to investigate the surface chemical states and composition. The XPS survey of the as-obtained MoO_2@C (Fig. 1b) reveals only Mo, O, and C, further demonstrating the high purity of the resultant MoO_2@C. The high-resolution Mo 3d spectrum (Fig. 1c) contains two strong peaks at 230.1 and 233.2 eV, which are related to Mo $3d_{5/2}$ and Mo $3d_{3/2}$ state of Mo^{4+}. The weak peak at 227.5 eV reveals trace amounts of metallic Mo. The C 1s spectrum (Fig. 1d), with one strong peak at 283.7 eV (sp^2 carbon) and one weak peak at 286.6 eV (sp^3 carbon), indicates the presence of carbon in the as-obtained MoO_2@C sample.

Morphological and textural information of the MoO_3 precursor and the MoO_2@C were acquired using SEM and TEM (Fig. 2). Before the calcination, MoO_3 shows a rod-like structure with a typical diameter of 200 nm (Fig. 2a) and various lengths (1-8 μm, Fig. S1, Supporting information). For the calcined sample (Fig. 2b), the original morphologies are well maintained. This one-dimensional (1D) structure can facilitate contact between the electrolyte and the anode material, and shorten the distance for Li^+ diffusion. After the calcination, uniformly distributed pores (highlighted in Fig. 2d) were observed, which were absent from the smooth surface of the starting MoO_3 (Fig. 2c). HR-TEM image of the MoO_3 (Fig. 2e) reveals some well-distributed lattice fringes with a d-spacing of 0.37 nm, which is related to the d_{100} of the orthorhombic α-MoO_3. For the calcined sample (Fig. 2f), a *d*-spacing of 0.34 nm was observed and assigned to the (011) planes of the monoclinic MoO_2, further confirming the reduction from the MoO_3 to the MoO_2. In addition, carbon layers (dashed rectangle in Fig. 2f), about 3 nm in width, were also observed in the MoO_2@C sample. The inter-planar spacing of 0.33 nm is related to the (002) planes of the carbon coating. The elemental mappings (Fig. 2g) indicate that all these three elements, Mo, O, and C, are homogeneously distributed. Therefore, it is reasonable to conclude that with the assistance of oleic acid, MoO_3 was

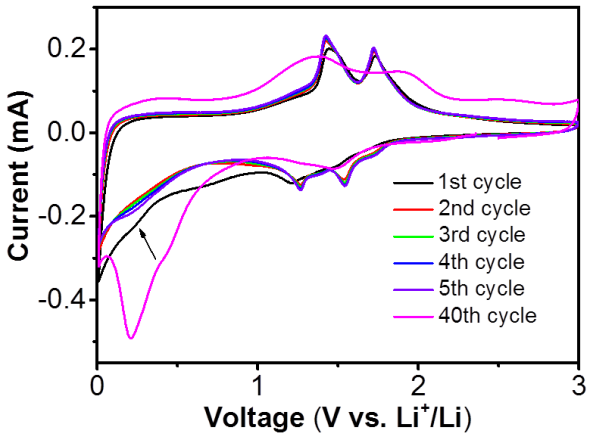

Fig. 4 Selected CVs of the Li/MoO_2@C at a scan rate of 0.1 mV s^{-1}, in the voltage range of 0.01-3.0 V vs. Li^+/Li.

simultaneously reduced into nanocrystals MoO_2 which were further coated with carbon layers. The carbon content of the MoO_2@C was evaluated by TGA (Fig. S2). The slight weight loss before 200 °C is likely caused by desorption of gas molecules. The weight loss between 300-415 °C is due to carbon combustion, which overwhelms the simultaneous weight gain caused by the oxidation of MoO_2 to MoO_3.[15] The weight then gradually increased to 95.5 wt % of the initial value and levels off. Based upon these figures, the MoO_2 and carbon weight contents are evaluated to be 84.9 and 15.1 wt %, respectively, in the composite. The formation mechanism for this MoO_2@C hybrid is illustrated in Fig. 2h. The hydrothermal reaction (step 1) leads to the formation of MoO_3 rods as evidenced by the SEM and XRD. After soaking in oleic acid for 24 h (step 2), the MoO_3 is coated by a thin layer of oleic acid. The followed annealing process (step 3) is crucial. When heated at 500 °C under Ar, oleic acid decomposes into carbon and releases some reducing gases (C_xH_y, H_2 etc.).[36, 37] The reduction under these conditions is not destructive, so the 1D rod shape, inherited from the precursor, is still maintained. The release of H_2O and CO_2 molecules from inside the 1D rod during the reduction would cause the formation of pores. As confirmed by the N_2 adsorption-desorption isothermas (Fig. 3). A type-IV hysteresis loop is observed in the MoO_2@C sample, indicative of the mesoporous nature. The Brunauer-Emmett-Teller (BET) surface area of the MoO_2@C is 45.7 m^2 g^{-1}, higher than that of commercial MoO_2 and the MoO_3 precursor (listed in Table 1). The MoO_2@C has an average pore size of 3.8 nm.

Electrochemical performance

The electrochemical performance of this MoO_2@C composite was investigated to study its potential as an anode material for LIBs. To explain its lithium storage mechanism, CV curves (CVs) of selected cycles are presented (Fig. 4). Two pairs of redox peaks, located at about 1.21/1.43 V and 1.48/1.73 V, were observed in the initial five cycles. These peaks could be attributed to the transformation between monoclinic MoO_2 phase and orthorhombic phase of the partially lithiated Li_xMoO_2 ($0 < x \leq 0.98$).[19, 23] The small peak located at lower potential (about 0.24 V) is likely related to the conversion reaction from MoO_2 to Mo. The intensity of this peak grows with cycling and becomes dominant in the 40th cycle, which indicates the transformation from an insertion−dominated to a conversion−dominated process.[14, 32]

Charge-discharge profiles of the MoO_2@C electrode at 0.5 A·g^{-1} were used to investigate its typical electrochemical properties (Fig. 5a). For the first cycle, the discharge and charge capacity was 701 and 468 mAh·g^{-1}, respectively. The large capacity loss is due to the irreversible side reactions, such as the formation of a solid electrolyte interphase film (SEI film, caused by the decomposition of the electrolyte), and the irreversible trapping of lithium ions by the MoO_2 lattice and disordered carbon.[23] The discharge and charge capacity then gradually increased to 955 and 948 mAh·g^{-1}, respectively, from the 40th cycle onward. This capacity increase is ascribed to two reasons: (1) the gradually formed gel−like polymer at the interface between electrode and electrolyte;[38, 39] (2) the transformation from insertion to conversion dominated process, which has a much higher capacity.[14, 40] Two pairs of short plateaus at about 1.49/1.73 V and 1.28/1.44 V were observed in the first discharge/charge profile, which agrees with CV results. During the cycling, however, these short platforms diminished after 40 cycles, further indicating the change from an insertion-dominated to a conversion-dominated process.[14, 23]

For the commercial MoO_2, which are composed of large particles with high purity (Fig. S3), a low capacity of 231 and 162 mAh·g^{-1} for the 1st and the 50th cycle was obtained, respectively. The obvious plateaus during the cycling indicate that the lithium storage occurred according to a one-electron insertion process, and the conversion reaction did not occur even after 140 cycles (Fig. S4). There is a significant difference in the contribution to capacity between the commercial MoO_2 and the as-obtained MoO_2@C electrodes at lower potential (< 1.0 V), especially below 0.75 V. This contribution is much lower for the commercial MoO_2 (~85 mAh·g^{-1}) than for the MoO_2@C electrode (~730 mAh·g^{-1}). The high reversible capacity of the

Cite this: DOI: 10.1039/c0xx00000x

www.rsc.org/xxxxxx

ARTICLE TYPE

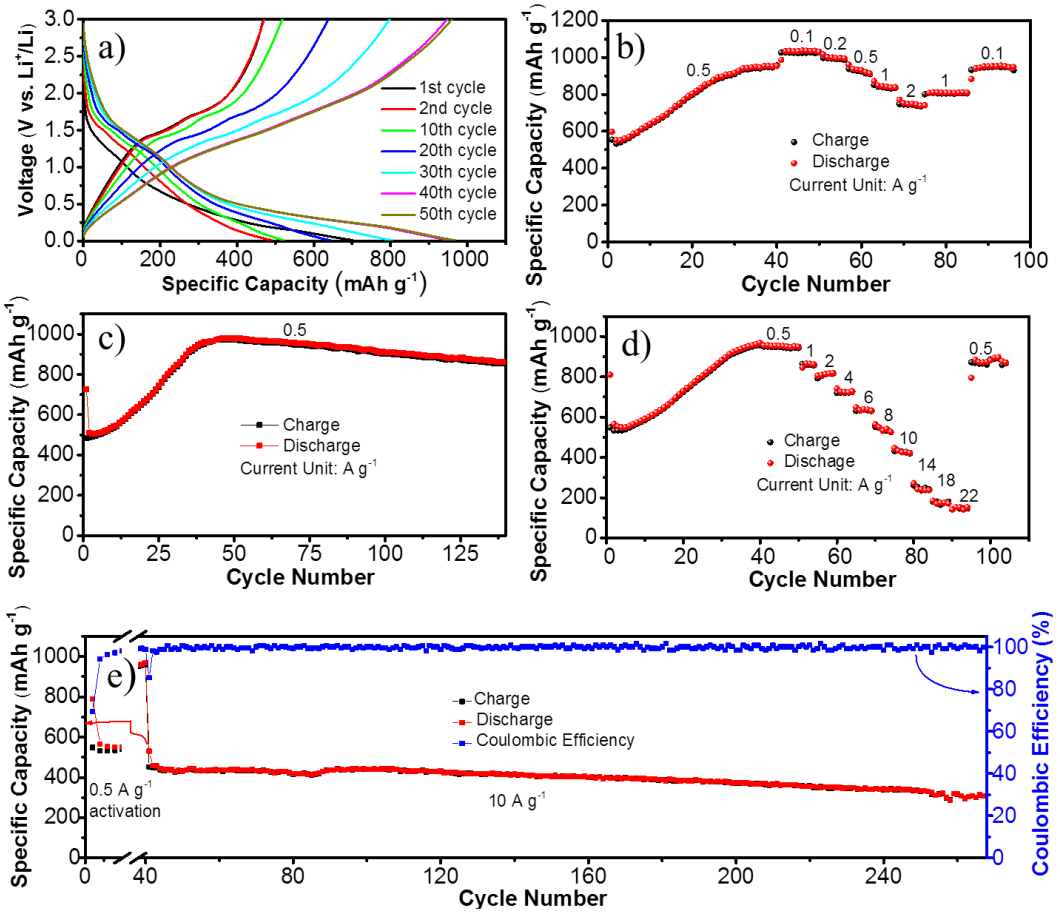

Fig. 5 Electrochemical performance of the as-obtained MoO_2@C as LIB anode. (a) Charge-discharge profiles for selected cycles at a specific current of 0.5 $A \cdot g^{-1}$, (b) low rate capability plots at various specific currents (0.1−1 $A \cdot g^{-1}$), (c) constant current cycling stability at 0.5 $A \cdot g^{-1}$, (d) high rate capability plots at various specific currents (0.5-22 $A \cdot g^{-1}$), and (e) long-life cycling stability and CE curves at a high current of 10 $A \cdot g^{-1}$.

MoO_2@C electrode at low potential was attributed to three reasons: formation of the gel-like polymer at the interface of the electrode and electrolyte, which is caused by the decomposition of electrolyte in the MO/Li cells;[38, 39] the four-electron conversion-dominated process in nanocrystal MoO_2[14]; and the insertion/de-insertion of Li^+ between the carbon layers.[18] Typical cycling performance of the MoO_2@C electrode at 0.5 $A \cdot g^{-1}$ (Fig. S5) shows a gradual increase in capacity that reaches the maximum after 40 cycles. Based on the above results, it is believed that the activation process of the MoO_2@C electrode can be completed within 40 cycles. Therefore, all the other electrochemical performances in Fig. 5 are tested with 40 cycles activation at 0.5 $A \cdot g^{-1}$.

The rate capability of the as-obtained MoO_2@C was first tested under low specific currents (varying from 0.1 to 1 $A \cdot g^{-1}$, Fig. 5b), and the performance of commercial MoO_2 was tested under the same conditions for comparison (Fig. S6). The charge−discharge curves of the MoO_2@C at 0.1 $A \cdot g^{-1}$ (after the activation, Fig. S7) display an average capacity of 1034 and 1026 $mAh \cdot g^{-1}$. With increasing the current to 0.2, 1, and 2 $A \cdot g^{-1}$, the electrode delivered a capacity of 990, 838, and 745 $mAh \cdot g^{-1}$, respectively. When dropped the current back to 0.1 $A \cdot g^{-1}$, the MoO_2@C electrode could still deliver a high reversible capacity of 956 $mAh \cdot g^{-1}$. The capacity of the MoO_2@C electrode is much higher than most of the reported MoO_2-based electrode and the theoretical capacity of nanostructured MoO_2 (838 $mAh \cdot g^{-1}$ for four-electron conversion).[16-18, 23, 41] The extra capacity can be attributed to the following factors: the structural defects in MoO_2@C, and the reversible lithium insertion/de-insertion into/from the carbon layers.[32] The commercial MoO_2, however, only showed a low capacity of 208, 197, 150, and 121 $mAh \cdot g^{-1}$ under specific currents of 0.1, 0.2, 1 and 2 $A \cdot g^{-1}$, respectively. The long-life cycling stability of the MoO_2@C at 0.5 $A \cdot g^{-1}$ specific current (Fig. 5c) is also excellent, showing a capacity of 861 $mAh \cdot g^{-1}$ even after 140 cycles. In contrast, the retained capacity of the commercial MoO_2 is only 134 $mAh \cdot g^{-1}$ under the same conditions (Fig. S6b). The MoO_2@C electrode can also maintain high capacities at higher currents (Fig. 5d), delivering a

discharge capacity of 720, 547, 260, and 180 mAh·g^{-1} at 4, 8, 14, and 18 A·g^{-1}, respectively. Even at a super-high specific current of 22 A·g^{-1}, the electrode can still deliver 155 mAh·g^{-1} capacity. The excellent rate capability, cycling stability, and high capacity of MoO_2@C electrode are much better than those in the literature (Table S1). More importantly, after charge-discharge at high current for 95 cycles, a capacity of 895 mAh·g^{-1} was achieved when the current was brought back to 0.5 A·g^{-1}. Therefore, the as-obtained MoO_2@C has superior reversibility. Fig. 5e displays the constant current cycling stability at 10 A·g^{-1}. After 268 cycles, a high capacity of 312 mAh·g^{-1} was still achieved, indicating a very low capacity decay of 0.54 mAh·g^{-1} per cycle. In addition, the Coulombic efficiency (CE) levels off at about 99.9 % up to the end of 268 cycles.

Electrochemical impedance spectroscopy (EIS) is very useful for examining the interfacial processes and kinetics of the electrode. In the Nyquist plots (Fig. S8) of the as-assembled cells, both the commercial MoO_2 and the MoO_2@C showed a depressed semicircle (related to the charge-transfer process) and one oblique straight line (representing typical Warburg impedance). The diameter of the depressed semicircle on the Z′ axis is related to the charge-transfer resistance value. Obviously, the charge-transfer resistance of the bulk MoO_2 is much larger than that of the MoO_2@C electrode. To further evaluate the electrochemical processes of the MoO_2@C, EIS curves at different cycles were also collected (Fig. 5). Besides the typical semicircle and inclined line, an extra semicircle (caused by the formation of the SEI film) is observed in the high-frequency range. An equivalent electric circuit was constructed to extract the resistance related to the electrolyte (R_s), charge-transfer (R_{CT}), the SEI caused charge-transfer resistance in the electrolyte-electrode interface (R_{SEI}), the constant phase elements (CPE), and the Warburg impedance (W), which corresponds to the Li^+ diffusion. Clearly, R_s stays almost the same during the cycling. As shown inset in Fig. 6, the slightly increasing R_{SEI} values indicate the decomposition of electrolyte during the cycling, which is common for conversion reactions.[39] The R_{CT}, however, continuously decreased from the 5th cycle to the 140th cycle, indicating the faster kinetics during the conversion process.

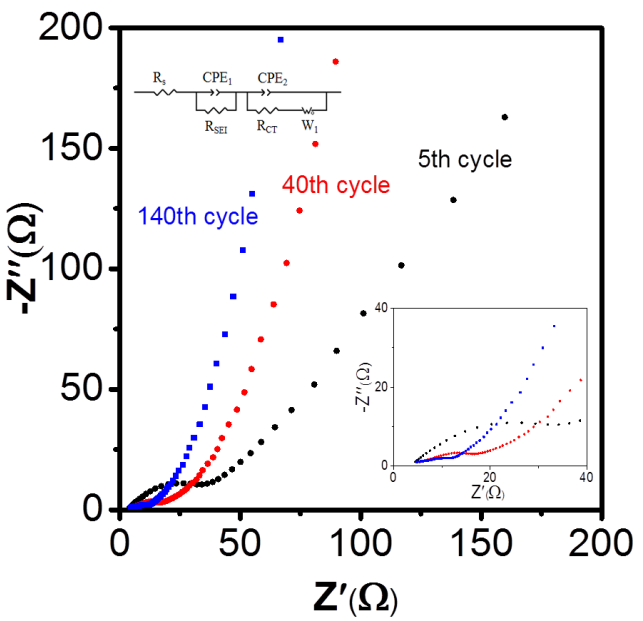

Fig.6 Nyquist plots of MoO_2@C electrode at selected cycles (full charged state). Insets are the corresponding equivalent circuit and the enlarged view at high-frequency range.

The superior electrochemical performance of this MoO_2@C electrode may have originated from the unique mesoporous 1D structure of the MoO_2@C nanocomposite. Previous reports have confirmed that nano-sizing MoO_2 can effectively alter its lithium-ion storage mechanism from one-electron insertion/de-insertion to the four-electron conversion reaction, which results in higher capacities.[20] The thin carbon coating can not only improve the conductivity, but also effectively buffer the volume change during cycling. The mesopores in the 1D structure also contribute to better contact between the electrolyte and the electrode.

Conclusions

In summary, we developed an effective method to synthesize MoO_2@C rods using oleic acid as both the reductant and carbon source. The as-obtained MoO_2@C rods have an average diameter of 200 nm and various lengths, and the carbon layers are a few nanometers thick. When applied as anode for LIBs, this nanocomposite exhibits remarkable electrochemical performance with super-high rate capability, high capacity, and long-term cycling stability. For example, a capacity of 1034, 720, 547, 260, and 180 mAh·g^{-1} was delivered at 0.1, 4, 8, 14, and 18 A·g^{-1}, respectively. Even at a high specific current of 22 A·g^{-1}, 155 mAh·g^{-1} capacity can be maintained. In addition, the cycling stability has also been improved, with capacities of 864 and 312 mAh·g^{-1} still retained after 140 and 268 cycles at 0.5 and 10 A·g^{-1}, respectively. All these improvements demonstrate that the MoO_2@C could be promising for high-performance, especially high-rate, LIBs.

Acknowledgments

This work was financially supported by grants from the 973 Program (China) (2011CB935900), the National Science Foundation of China (NSFC) (21231005), the Ministry of Education (MOE) of China (IRT13R30), the 111 Project (B12015), the Research Fund for the Doctoral Program of Higher Education of China (20120031110001), and the Tianjin Science & Technology Project (10SYSYJC27600). Y. Wang thanks the China Scholarship Council (CSC) for scholarship support. This research used equipment funded by the Australian Research Council (ARC) through a Linkage, Infrastructure, Equipment and Facilities (LIEF) grant (LE120100104) for facilities located at the UOW Electron Microscopy Centre. The authors would like to thank Dr. Tania Silver for critical reading of the manuscript.

Notes and references

[a] *Key Laboratory of Advanced Energy Materials Chemistry (MOE), Collaborative Innovation Centre of Chemical Science and Engineering (Tianjin), Nankai University, Tianjin 300071, China. Fax/Tel: +86 22 23503639; E-mail: wangyj@nankai.edu.cn.*

[b] *Institute for Superconducting and Electronic Materials, University of Wollongong, Wollongong, NSW 2522, Australia. Fax: +61 2 4221 5731; Tel: +61 2 4221 3220; E-mail: zhenguo@uow.edu.au*

† Electronic Supplementary Information (ESI) available: See DOI: 10.1039/b000000x/

1. A. S. Arico, P. Bruce, B. Scrosati, J.-M. Tarascon and W. van Schalkwijk, *Nat. Mater.*, 2005, **4**, 366-377.
2. K. Kang, Y. S. Meng, J. Bréger, C. P. Grey and G. Ceder, *Science*, 2006, **311**, 977-980.
3. Q. Zhang, E. Uchaker, S. L. Candelaria and G. Cao, *Chem. Soci. Rev.*, 2013, **42**, 3127-3171.
4. T. Stephenson, Z. Li, B. Olsen and D. Mitlin, *Energy Environ. Sci.*, 2014, **7**, 209-231.
5. M. D. Bhatt and C. O'Dwyer, *Phys. Chem. Chem. Phys.*, 2015, **17**, 4799-4844.
6. Y. Hu and X. Sun, *J. Mater. Chem. A*, 2014, **2**, 10712-10738.
7. H. Li, Z. Wang, L. Chen and X. Huang, *Adv. Mater.*, 2009, **21**, 4593-4607.
8. M. V. Reddy, G. V. Subba Rao and B. V. R. Chowdari, *Chem. Rev.*, 2013, **113**, 5364-5457.
9. K. Zhang, X. Han, Z. Hu, X. Zhang, Z. Tao and J. Chen, *Chem. Soci. Rev.*, 2015, **44**, 699-728.
10. J. P. Paraknowitsch and A. Thomas, *Energy Environ. Sci.*, 2013, **6**, 2839-2855.
11. B. J. Landi, M. J. Ganter, C. D. Cress, R. A. DiLeo and R. P. Raffaelle, *Energy & Environmental Science*, 2009, **2**, 638-654.
12. M. N. Obrovac and V. L. Chevrier, *Chem. Rev.*, 2014, **114**, 11444-11502.
13. C.-M. Park, J.-H. Kim, H. Kim and H.-J. Sohn, *Chem. Soci. Rev.*, 2010, **39**, 3115-3141.
14. B. Guo, X. Fang, B. Li, Y. Shi, C. Ouyang, Y.-S. Hu, Z. Wang, G. D. Stucky and L. Chen, *Chem. Mater.*, 2012, **24**, 457-463.
15. L. Guo and Y. Wang, *J. Mater. Chem. A*, 2015, **3**, 4706-4715.
16. A. Chen, C. Li, R. Tang, L. Yin and Y. Qi, *Phys. Chem. Chem. Phys.*, 2013, **15**, 13601-13610.
17. S. Hu, F. Yin, E. Uchaker, W. Chen, M. Zhang, J. Zhou, Y. Qi and G. Cao, *J. Phys. Chem. C*, 2014, **118**, 24890-24897.
18. Z. X. Huang, Y. Wang, Y. G. Zhu, Y. Shi, J. I. Wong and H. Y. Yang, *Nanoscale*, 2014, **6**, 9839-9845.
19. J. R. Dahn and W. R. McKinnon, *Solid State Ionics*, 1987, **23**, 1-7.
20. X. Hu, W. Zhang, X. Liu, Y. Mei and Y. Huang, *Chem. Soc. Rev.*, 2015, **44**, 2376-2404.
21. P. Roy and S. K. Srivastava, *J. Mater. Chem. A*, 2015, **3**, 2454-2484.
22. Y. Sun, X. Hu, W. Luo and Y. Huang, *ACS Nano*, 2011, **5**, 7100-7107.
23. H.-J. Zhang, J. Shu, K.-X. Wang, X.-T. Chen, Y.-M. Jiang, X. Wei and J.-S. Chen, *J. Mater. Chem. A*, 2014, **2**, 80-86.
24. Y. Sun, X. Hu, W. Luo and Y. Huang, *J. Mater. Chem.*, 2012, **22**, 425-431.
25. D. Koziej, M. D. Rossell, B. Ludi, A. Hintennach, P. Novák, J.-D. Grunwaldt and M. Niederberger, *Small*, 2011, **7**, 377-387.
26. X. Zhang, X. Song, S. Gao, Y. Xu, X. Cheng, H. Zhao and L. Huo, *J. Mater. Chem. A*, 2013, **1**, 6858-6864.
27. H.-J. Zhang, T.-H. Wu, K.-X. Wang, X.-Y. Wu, X.-T. Chen, Y.-M. Jiang, X. Wei and J.-S. Chen, *J. Mater. Chem. A*, 2013, **1**, 12038-12043.
28. Z. Wang, J. S. Chen, T. Zhu, S. Madhavi and X. W. Lou, *Chem. Commun.*, 2010, **46**, 6906-6908.
29. X. Liu, W. Ji, J. Liang, L. Peng and W. Hou, *Phys. Chem. Chem. Phys.*, 2014, **16**, 20570-20577.
30. X. Zhao, M. Cao, B. Liu, Y. Tian and C. Hu, *J. Mater. Chem.*, 2012, **22**, 13334-13340.
31. L. Zhou, H. B. Wu, Z. Wang and X. W. Lou, *ACS Appl. Mater. interfaces*, 2011, **3**, 4853-4857.
32. W. Tang, C. X. Peng, C. T. Nai, J. Su, Y. P. Liu, M. V. Reddy, M. Lin and K. P. Loh, *Small*, 2015, **11**, 2446-2453.
33. L. Zeng, C. Zheng, C. Deng, X. Ding and M. Wei, *ACS Appl. Mater. Interfaces*, 2013, **5**, 2182-2187.
34. X. W. Lou and H. C. Zeng, *Chem. Mater.*, 2002, **14**, 4781-4789.
35. N.-S. Choi, Y. Lee, S.-S. Kim, S.-C. Shin and Y.-M. Kang, *J. Power Sources*, 2010, **195**, 2368-2371.
36. D. G. Lima, V. C. D. Soares, E. B. Ribeiro, D. A. Carvalho, É. C. V. Cardoso, F. C. Rassi, K. C. Mundim, J. C. Rubim and P. A. Z. Suarez, *J. Anal. Appl. Pyrolysis*, 2004, **71**, 987-996.
37. Z. Xu, C. Shen, Y. Hou, H. Gao and S. Sun, *Chem. Mater.*, 2009, **21**, 1778-1780.
38. J. M. Tarascon and M. Armand, *Nature*, 2001, **414**, 359-367.
39. S. Laruelle, S. Grugeon, P. Poizot, M. Dollé, L. Dupont and J. M. Tarascon, *J. Electrochem. Soc.* 2002, **149**, A627.
40. L. C. Yang, Q. S. Gao, Y. H. Zhang, Y. Tang and Y. P. Wu, *Electrochem. Commun.* 2008, **10**, 118-122.
41. H. Yu, Y. Ren, D. Xiao, S. Guo, Y. Zhu, Y. Qian, L. Gu and H. Zhou, *Angew Chem. Int. Ed. Engl.*, 2014, **53**, 8963-8969.